Chemical Engineering Journal 519 (2025) 165308

Contents lists available at ScienceDirect

Chemical Engineering Journal

journal homepage: www.elsevier.com/locate/cej

Computational fluid dynamics investigation of CO_2 absorption using ionic liquids in hollow-fiber membrane contactors

Alexandru-Constantin Bozonc [a], Lucía Gómez-Coma [b], Guillermo Díaz-Sainz [b], Angel Irabien [b], Ana-Maria Cormos [a,*]

[a] Faculty of Chemistry and Chemical Engineering, Babes-Bolyai University, 11 Arany-Janos, 400028 Cluj-Napoca, Romania
[b] Departamento de Ingenierías Química y Biomolecular, Universidad de Cantabria, Avenida de los Castros s/n, 39005 Santander, Spain

ARTICLE INFO

Keywords:
CO_2 capture
CFD
HFMC
Ionic liquids
Nondispersive absorption
Mathematical modeling

ABSTRACT

This study integrates computational fluid dynamics (CFD) modeling with previously obtained experimental data to investigate the CO_2 absorption process using hollow fiber membrane contactors (HFMCs) and ionic liquids (ILs). Two types of HFMCs, polysulfone (PS) and polypropylene (PP), were tested in combination with two ILs: [emim][Ac] and [emim][$EtSO_4$]. The CFD models, developed using COMSOL Multiphysics, were validated against laboratory-scale experimental data. A strong correlation between the experimental and simulated results was observed, as indicated by high R^2 values (0.9208 to 0.9844) and low RMSE values (1.4657 to 2.1479), confirming the model's accuracy in representing the actual process. Among the ILs studied, [emim][Ac] showed superior CO_2 absorption efficiency due to its higher CO_2 solubility compared to [emim][$EtSO_4$]. Velocity and concentration profiles of both gas and liquid phases were determined, showcasing the ability of CFD modeling to predict key process parameters across the system geometry. Sensitivity analyses identified the optimal absorption temperature, membrane length, and gas velocity to achieve CO_2 absorption efficiency exceeding 90 %. Results showed that increasing the absorption temperature and membrane length significantly enhances the process performance. Additionally, incorporating shell baffles improved absorption efficiency by approximately 5 %, though it resulted in a notable increase in liquid pressure drop across the shell.

1. Introduction

The continuing rise in greenhouse gas (GHG) emissions from human activities has significantly intensified global warming [1]. Carbon dioxide (CO_2) emissions account for approximately 60% of the total impact on global warming, with 86% of those emissions coming from anthropogenic sources [2]. One of the key solutions for reducing the amount of CO_2 emissions into the atmosphere is carbon capture, utilization, and storage (CCUS) [3,4]. Among all carbon capture methods, post-combination technologies are the most viable to be implemented, as CO_2 separation occurs after the combustion of fuels (such as fossil fuels or biomass). Chemical absorption using alkanolamines, such as monoethanolamine (MEA), is the most commonly employed gas-liquid absorption process in industrial applications [5], primarily due to its rapid absorption rate and high CO_2 capture efficiency.

However, the use of MEA as a liquid solvent comes with a series of disadvantages. Those include high energy consumption for thermal regeneration, the MEA is also subjected to oxidation with various chemicals (i.e., O_2 and SO_2), increased viscosity at higher concentrations, and a high corrosion potential [6,7]. These limitations can be mitigated by mixing the MEA with various substances, such as ionic liquids (IL) or glycerol. These blends can reduce the volatility of MEA, increase the solubility of CO_2, and reduce the corrosion potential and high energy requirements for solvent regeneration [8].

Conventionally, post-combustion absorption of CO_2 is carried out in packed-bed columns [9]. These systems face various operational challenges, such as channeling, foaming, entraining, flooding, poor heat transfer, and significant pressure drops [10,11]. To address these issues, hollow fiber membrane contactors (HFMCs) offer a promising alternative for CO_2 capture [12]. This technology provides a series of advantages over the conventional one, such as: i) the mass transfer area is significantly increased by the large number of membranes; ii) some of the operation problems (i.e., foaming, flooding, channeling, and entraining) are avoided due to the separation of the two phases; iii)

* Corresponding author.
E-mail address: ana.cormos@ubbcluj.ro (A.-M. Cormos).

https://doi.org/10.1016/j.cej.2025.165308
Received 16 January 2025; Received in revised form 26 May 2025; Accepted 23 June 2025
Available online 24 June 2025

simpler scale up, due to the high modularity of the membranes; iv) reduced loss of solvent due to evaporation and entraining effect, resulting in a more environmental friendly process; v) lower investment and operational costs; vi) low solvent hold-up, advantages when using high expensive solvents [13–18].

However, HFMCs also present challenges, including: i) additional resistance to CO_2 mass transfer due to the membrane; ii) limited membrane lifetime, requiring periodic replacement; iii) potential wetting of the membranes, which reduces process efficiency over time; iv) difficulties in producing small-diameter membranes [15,16,19]. ILs have emerged as alternative solvents in HFMC systems, addressing the limitations of conventional packed-bed columns and MEA absorbent solution.

ILs, primarily salts composed of asymmetric organic cations and organic or inorganic anions [11] are broadly categorized into: (i) room-temperature ILs (RTILs) and (ii) task-specific ILs (TSILs). The key difference between these two groups in CO_2 capture lies in the nature of the CO_2-IL interaction. RTILs primarily exhibit physical absorption, while TSILs facilitate both physico and chemical interactions, enhancing CO_2 loading capacity. However, TSILs often face challenges during regeneration, as breaking the chemical bonds between CO_2 and the IL requires significant energy [20,21].

The main characteristics of ILs are their low volatility, thermal stability, and flexibility in formulation and manufacturing, which give them advantages over other absorbents [22,23]. However, some drawbacks of most ILs include their high cost and viscosity. Increased viscosity can reduce the diffusion rate of CO_2 in the IL, which diminishes mass transfer and complicates their use as absorbents in capture processes [24]. To avoid the complex procedures involved in calculating IL properties due to their flexible design, advanced computer modeling and molecular simulation programs are often used to estimate physicochemical properties such as CO_2 solubility in ILs [25,26].

Currently, two main trends have emerged in the evaluation of the desorption process using vacuum-assisted membrane technology and ILs: (i) the study of membrane-IL compatibility, as reported by Bazhenov et al. [27] and Mulukutla et al. [28], and (ii) the analysis, modeling, and simulation of the process, addressed in recent works by, Simons et al. [24], Lu et al. [29], and Vadillo et al. [30].

It is also noteworthy that different classes of solvents, such as amine-based solvents, IL-based solvents, amino acid-based ILs, and deep eutectic solvents (DES) can be effectively employed in HFMCs for CO_2 capture.

For instance, Xia et al. developed a two-dimensional, steady-state, non-wetting model for CO_2 absorption in HFMCs using aqueous ammonia, MEA, and diethanolamine (DEA). Their results showed that aqueous ammonia achieved CO_2 removal efficiencies above 95%, outperforming MEA and DEA when the CO_2 volume fraction exceeded 19% [18]. Similarly, Zhang et al. demonstrated that MEA-based systems in HFMCs could reach absorption efficiencies up to 90% at optimal MEA concentrations. For a gas stream containing 10% CO_2, removal efficiencies ranged from 85% to 90% [31].

Regarding IL-based solvents, Qazi et al. investigated the performance of [emim][OAc], [emim][$EtSO_4$], and [emim][$MeSO_4$] in HFMCs. Their findings indicated that [emim][OAc] delivered the highest CO_2 absorption efficiency, achieving a mass transfer coefficient of 7.6×10^{-6} m/s and removal efficiencies exceeding 90% under optimal conditions. These results highlighted the critical influence of IL solubility and viscosity on CO_2 capture performance [30].

In the category of amino acid-based ILs, Jafari et al. assessed cholinium lysinate ([Cho][Lys]) for CO_2 absorption in HFMCs, achieving an efficiency of 85% under optimized conditions. The high performance was attributed to the IL's polar nature and strong interactions with CO_2 molecule [32].

Finally, Zhang et al. explored the use of reline—a deep eutectic solvent—for CO_2 capture in HFMCs. They reported a removal efficiency of 96.9% from a gas mixture containing 50 mol% CO_2 and 50 mol% N_2 at a feed pressure of 4 bar, along with a flux of 67.43 mmol/(m^2h), demonstrating the high potential of DES-based systems for efficient CO_2 separation [33].

Despite progress in the modeling of membrane-based gas absorption, there remains a lack of detailed 3D CFD studies that are both experimentally validated and capable of capturing the complex flow and mass transfer behavior of IL systems at different temperatures in HFMCs. In this work, we investigate CO_2 absorption using two ILs (i.e., 1-Ethyl-3-methylimidazolium acetate ([emim][Ac]) and 1-Ethyl-3-methylimidazolium ethylsulfate ([emim][EtSO4]), in two types of HFMCs (i.e., polysulfone (PS) and polypropylene (PP)). An integrated approach combining innovative 3D computational fluid dynamics modeling with previously obtained experimental data is employed in this study. Experimental data validate the mathematical models, which are then used to analyze velocity and concentration profiles in the gas and liquid phases. Sensitivity analyses assess the effects of membrane characteristics (e.g., length) and fluid velocities on absorption efficiency. Finally, the performance of conventional HFMC design is compared with alternative configurations featuring distinct shell baffle geometries in order to increase the absorption efficiency. The comparison between the modeling and simulation results presented in this study is highly promising, demonstrating that high CO_2 absorption efficiencies can be achieved under various operating conditions.

2. Methodology

2.1. Materials

Carbon dioxide (99.7 ± 0.01 vol%) and pure nitrogen (99.999 ± 0.001 vol%) were purchased from Air Liquide (Spain). The gas stream used in the experiments consisted of 15% carbon dioxide and 85% nitrogen. The ILs were supplied by Sigma Aldrich. 1-Ethyl-3-methylimidazolium ethylsulfate [emim][$EtSO_4$] (⩾95%) was selected as the absorption liquid due to its low viscosity, low toxicity, and cost-effectiveness. In contrast, 1-Ethyl-3-methylimidazolium acetate [emim][Ac] (⩾90%) was chosen for its high CO_2 solubility. The PP HFMC was supplied by Liquicel-Membrane Contactors (USA), while the PS HFMC was provided by VWR International Eurolab, S.L. (Spain). Their key characteristics are summarized in Table 1.

The operating conditions for the HFMCs used in the absorption process are summarized in Table 2, where the temperature and gas composition were selected based on typical values observed in post-combustion processes, while the flow rates were chosen according to the recommended operating conditions provided by the manufacturers of PP and PS HFMCs.

2.2. Methods

The experimental setup is illustrated in Fig. 1. The feed gas mixture was regulated by a mass flow controller (Brook Instrument MFC 5850, Emerson Process Management, Spain). The gas stream passed through the interior of the hollow fibers, while liquid absorbent was circulated counter-currently in a closed loop through the shell side. This configuration was chosen for its superior absorption efficiency compared to the

Table 1
Characteristics of PP and PS HFMC [34,35].

Parameter	Unit	PP	PS
Fiber o.d. (d_o)	m	$3{\cdot}10^{-4}$	$1.3{\cdot}10^{-3}$
Fiber i.d. (d_i)	m	$2.2{\cdot}10^{-4}$	$7.0{\cdot}10^{-4}$
Fiber length (L)	m	0.115	0.347
Number of fibers (n)	–	2300	400
Shell diameter (D_s)	m	2.5×10^{-2}	4.5×10^{-2}
Porosity (ϵ_{mem})	%	40	43
Packing factor (φ_{mem})	–	0.39	0.43
Tortuosity ($\tau_{mem} = 1/\epsilon_{mem}$)	–	2.50	2.33

Table 2
Operating conditions of the absorption process.

Parameter	Unit	Value
Gas flow rate (F_g)	mL/min	70
Liquid flow rate (F_l)	mL/min	50
Absorption pressure (P)	atm	1
Temperature (T)	K	290–350
Gas composition	vol% CO_2	15
	vol% N_2	85

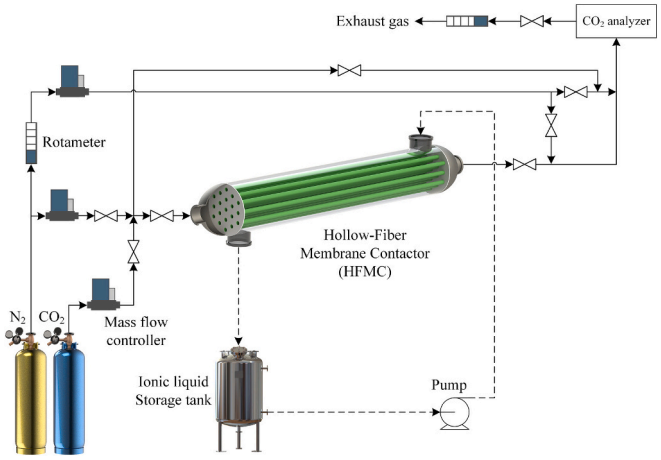

Fig. 1. Experimental set-up for laboratory-scale CO_2 capture system.

reverse arrangement (i.e., liquid inside the tubes and gas in the shell) [36]. HFMC acted as a physical barrier between the phases, enabling CO_2 to diffuse from the gas mixture into the IL through the membrane's permeable pores. The ILs were pumped from a storage tank, with liquid flow (50 mL/min) controlled by a digital gear pump (Cole Parmer Instrument Company, Hucoa-Erloss SA, Spain). Heating tapes were used to maintain isothermal conditions around the pipes.

Experiments were conducted at temperatures of 291 K, 298 K, 318 K, 333 K, and 348 K for each IL. Each experiment was repeated three times under identical conditions, and the average values were calculated.

The gas flow rate was maintained at 70 mL/min. The CO_2 concentration in the outlet gas stream was continuously monitored using a non-dispersive infrared (NDIR) spectroscopy analyzer (Emerson Process). Before analysis, the gas sample was diluted with additional N_2 to maintain the required concentration range for the NDIR analyzer (minimum flow of 200 mL/min). Steady-state conditions were achieved when the CO_2 concentration in the outlet gas stream remained constant.

3. Mathematical model approach

The 3D CFD models for CO_2 capture using ILs were developed and implemented in COMSOL Multiphysics. Based on the HFMCs characteristics presented in Table 1, the geometry of the PS HFMC is illustrated in Fig. 2. The PS HFMC comprises 400 hollow fibers distributed symmetrically within a shell compartment with an internal diameter of 4.5 cm. The system is divided into three regions: i) tubes (i.e., the space inside the membranes where the gas mixture flows), ii) polymeric membranes, and iii) shell (i.e., the space between the membranes where the liquid absorbent flows). CO_2 is absorbed from the gas phase through the membrane pores into the liquid solution, where it reacts with the IL, as depicted in Fig. 2. To optimize computational efficiency, the symmetry of the system was leveraged. Thus, only half of the geometry, shown in purple in Fig. 2, was simulated. This approach significantly reduced simulation time and computational demands while preserving the representativeness of the HFMC module. A similar modeling method was applied to the PP HFMC module.

The 3D CFD models for CO_2 absorption in ILs were implemented in COMSOL Multiphysics 6.2, using the finite element method (FEM) to solve the governing partial differential equations (PDEs). The accuracy of simulation results depends heavily on the discretization system (mesh). The mesh for the PS HFMC module is presented in Fig. 3. The geometry was divided into three sections, with a different mesh applied for each of them. Sections 1 and 3 are identical, except that the shell inlet/outlet are on opposite sides. The section planes (i.e., Plane 1, Plane 2, Plane 3, and Plane 4) that divide the three sections have a unified mesh, shown in the upper right of Fig. 3. This is a triangular mesh with a

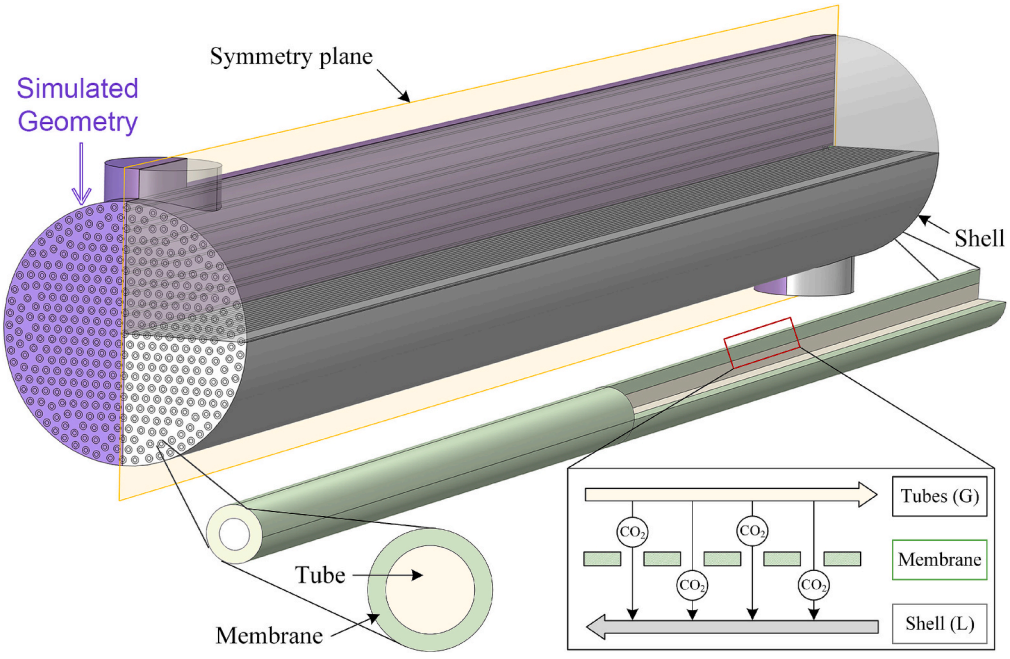

Fig. 2. Hollow-fiber PS membrane contactor geometry. (For interpretation of the references to color in this figure, the reader is referred to the web version of this article.)

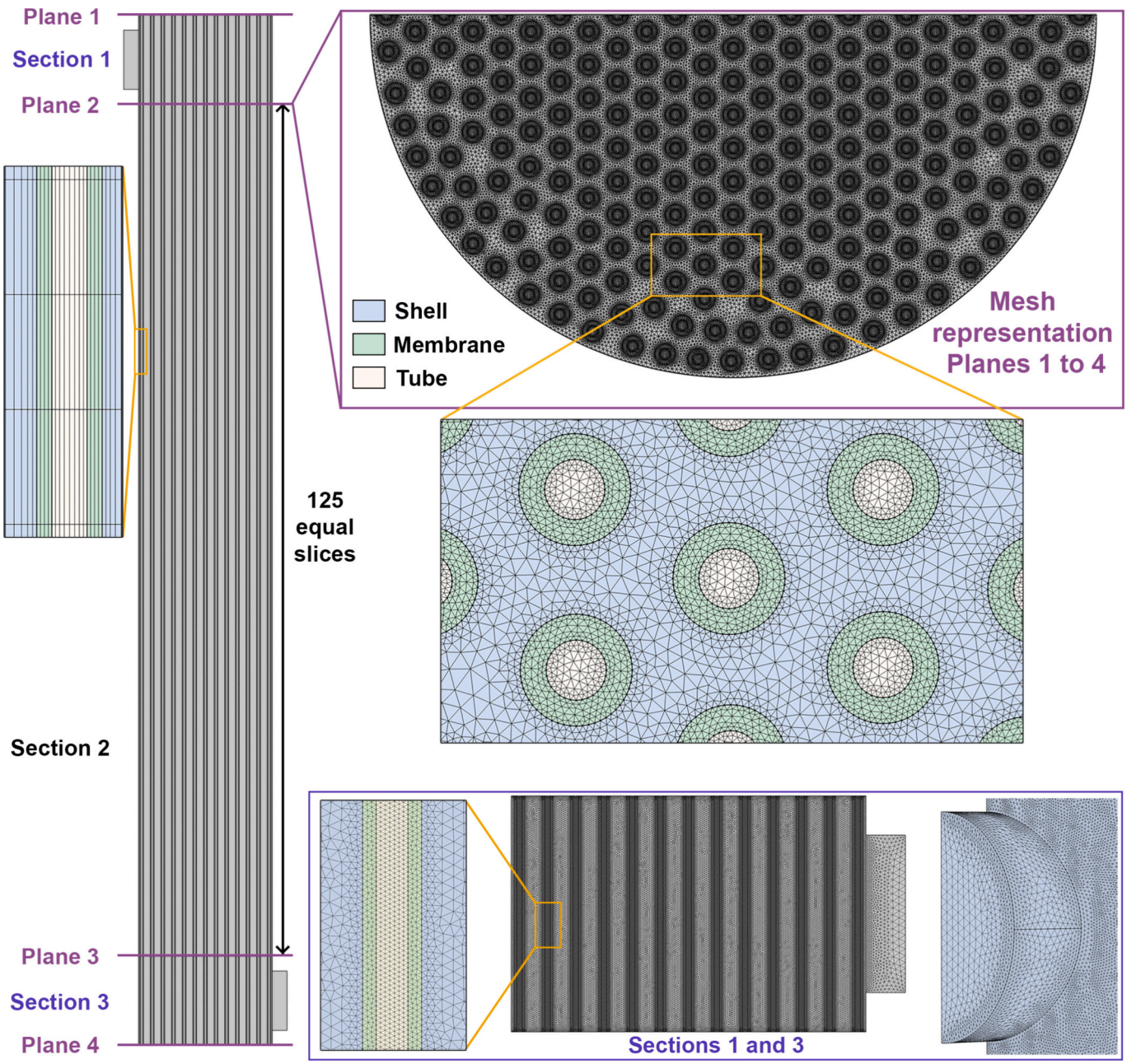

Fig. 3. Mesh employed for the PS HFMC module.

higher density of elements inside and around the membranes. The total number of mesh elements on a section plane is 183,812.

The geometry in Section 2 has been sliced into 125 equal pieces, each slice having a consistent mesh with that of Planes 2 and 3, with a total number of elements of 22,976,500. Due to the presence of an inlet/outlet shell connection, a different mesh was implemented for Sections 1 and 3. As shown at the bottom of Fig. 3, a tetrahedral distribution of the mesh is used. A higher mesh quality was considered for the membranes and the gas-liquid interface (outside of the membranes, at contact with the liquid in the shell). For the discretization of Sections 1 and 3, a number of 113,564,026 elements were required for each section (e.g., shell: 35,264,069, membranes: 55,347,184, and tubes: 22,952,773). The total number of elements for the implemented geometry is 250,104,552. The mesh used in the model was refined iteratively by gradually increasing the mesh quality until mesh convergence was achieved, as presented in the mesh convergence plot (Fig. 4), where the variation of steady state absorption efficiency at different number of mesh elements is presented. This ensured that the model produced results independent of further mesh adjustments.

The simulations were performed on a computer with a 64-bit operating system, two Intel(R) Xeon(R) Platinum 8168 CPUs running at 2.70 GHz, and 512 GB of DDR4 RAM at 2666 MHz.

The developed 3D mathematical models are implemented in dynamic conditions. The governing equations account for the conservation of momentum, mass, species concentrations, and temperature variations across the tubes, membranes, and shell regions.

3.1. Mass and momentum conservation equations

The conservation of mass for both phases is ensured by the following continuity equation:

$$\frac{\partial \rho_i}{\partial t} + \nabla \cdot (\rho u_i) = 0 \tag{1}$$

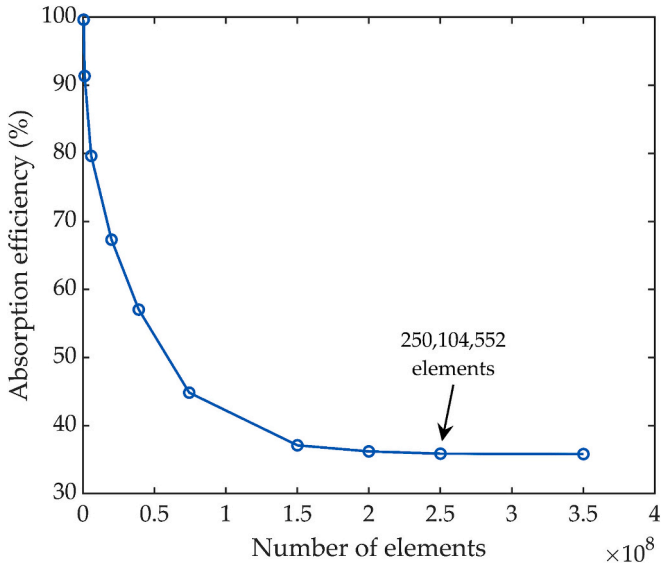

Fig. 4. Mesh sensitivity analysis.

The conservation of momentum for the two phases (i.e., gas and liquid) is implemented by the Navier-Stokes equation:

$$\rho_i \frac{\partial u_i}{\partial t} + \rho(u_i \cdot \nabla)u_i = \nabla \cdot (-\rho_i I + \tau_i) \tag{2}$$

The viscous stress tensor (τ_i) is calculated with:

$$\tau_i = \mu_i\left(\nabla u_i + (\nabla u_i)^T\right) - \frac{2}{3}\mu_i(\nabla \cdot u_i)I \tag{3}$$

3.2. Tubes governing equations

The gas mixture flows in the tubes, where mass transfer occurs via convection and diffusion under isotropic conditions, with no chemical reactions. Gas-phase concentration changes are described by Eq. (4).

$$\frac{\partial c_j}{\partial t} + \nabla \cdot \left(-D_j \nabla c_j\right) + u \cdot \nabla c_j = 0 \tag{4}$$

Heat transfer in the tubes (Eq. (5)) is influenced by convection, conduction, and heat exchange from the liquid phase, where the exothermic absorption in [emim][Ac] and [emim][$EtSO_4$] occurs [37].

$$\rho C_p \frac{\partial T}{\partial t} + \rho C_p u \cdot \nabla T + \nabla \cdot (-\lambda \nabla T) = Q_{transfer} \tag{5}$$

3.3. Membranes governing equations

Species diffusion through membrane pores is characterized by an effective diffusion coefficient, accounting for porosity and tortuosity:

$$\varepsilon_{mem} \frac{\partial c_j}{\partial t} + \nabla \cdot \left(-\frac{\varepsilon_{mem}}{\tau_{mem}} D_j \nabla c_j\right) + u \cdot \nabla c_j = 0 \tag{6}$$

Due to the membrane's small thickness (e.g., 40 μm for PP and 30 μm for PS), heat transfer is assumed to occur by conduction only, the following equation being used:

$$\rho C_p \frac{\partial T}{\partial t} + \nabla \cdot (-\lambda \nabla T) = Q_{transfer} \tag{7}$$

3.4. Shell governing equations

In the shell, mass transfer includes convection, diffusion, and the reaction of absorbed CO_2 with ILs. Therefore, the governing equation used to calculate the concentration variation of the species in the shell is presented below:

$$\frac{\partial c_j}{\partial t} + \nabla \cdot \left(-D_j \nabla c_j\right) + u \cdot \nabla c_j = \pm R_j \tag{8}$$

The reaction mechanism for CO_2 capture with ILs has been studied extensively by Zareiekordshouli et al. [38]. Given the high IL concentration, the variation of the IL concentration due to the reaction with the absorbed CO_2 is minimal, therefore the IL concentration around the gas-liquid interface remains constant. Allowing the use of a pseudo-first order reaction regarding CO_2. The reaction rate is expressed using the following equation [38]:

$$R_{CO_2} = k_0 \cdot c_{CO_2,liq} \tag{9}$$

The Arrhenius expression can be used to calculate the pseudo-first order reaction constant (k_0) at different temperatures, considering the activation energy of 10.317 kJ/mol and the frequency factor of 1545 1/s for [emim][Ac] [38]. In the case of the CO_2 reaction with [emim][$EtSO_4$], a reaction constant of 2.66 × 10^{-3} 1/s [39] at room temperature was used.

The Henry's law is applied in order to calculate the solubility of CO_2 in the ILs. The Henry's coefficient for CO_2 in the two ILs at different temperatures is calculated by applying the quadratic function presented in Eq. (10) [37], using the A_i coefficients for each IL, which are presented in Table 3.

$$\log(K_H) = A_0 + A_1 \cdot \left(\frac{1}{T}\right) - A_2 \cdot \left(\frac{1}{T}\right)^2 \tag{10}$$

The temperature changes of the liquid phase take into account, in addition to the conventional and conduction mechanisms, the heat of absorption, which is determined by the following equation:

$$\rho C_p \frac{\partial T}{\partial t} + \rho C_p u \cdot \nabla T + \nabla \cdot (-\lambda \nabla T) = Q_{absorption} - Q_{transfer} \tag{11}$$

3.5. Physico-chemical properties

Table 3 shows the main equations used to calculate the physico-chemical properties of ILs and gas mixture.

The difference in CO_2 concentration between the gas phase inlet and outlet is used to calculate the absorption efficiency of the process, using

Table 3
Physico-chemical properties of ILs and gas mixture.

Parameter	Unit	Ref.
IL: [emim][Ac]		
$\rho_{IL} = 1280.8 - 0.608 \cdot T$	kg/m^3	
$\log\mu_{IL} = -1.657 + \frac{673.7}{T - 196.1}$	mPa s	[40]
$D_{CO_2-IL} = 2.00 \cdot 10^{-3}\left(\frac{T}{\mu_{IL}}\right)^{0.6} \cdot v_{CO_2}^{-1.04}$	cm^2/s	[38]
$C_p = 1.18717 + 0.00591 \cdot T$	kJ/(kg K)	[41]
$\lambda = 0.27731 + 2.1846 \cdot 10^{-4} \cdot T$	W/(m K)	
$A_0 = -37.8926$, $A_1 = 25839.17$, $A_2 = -4280352$		[37]
IL: [emim][$EtSO_4$]		
$\rho_{IL} = 1.2541 - 5.98 \cdot 10^{-4} \cdot (T - 273.15)$	g/m^3	
$\mu_{IL} = 5.68 \cdot 10^{-3} \cdot T^{0.5} \exp\left(\frac{945}{T - 162}\right)$	mPa s	[42]
$D_{CO_2-IL} = 6.7 \cdot 10^{-5} \cdot \mu_{IL}^{-0.66} \cdot M_{IL}^{-0.89} \rho_{IL}^{4.8} \cdot T^{-3.3}$	cm^2/s	[37]
$C_p = 5.827 \cdot 10^2 - 6.161 \cdot 10^4 \cdot T^{-1}$	J/(mol K)	[43]
$\lambda = 0.195 - 3.35 \cdot 10^{-5} \cdot$T	W/(m K)	[44]
$A_0 = 58.94063$, $A_1 = -35093.1$, $A_2 = 5385315$		[37]
Gas mixture		
$\rho_g = \sum y_i \cdot \rho_i$	kg/m^3	[45]
$D_{CO_2-g} = 1.38 \cdot 10^{-5} \cdot \left(\frac{T}{273.15}\right)^{3/2}$	m^2/s	[46]

the following equation:

$$Absorption\ efficiency = \frac{C_{CO_2}^{in} - C_{CO_2}^{out}}{C_{CO_2}^{in}} \cdot 100 \quad (12)$$

4. Results and discussion

Using the HFMC characteristics listed in Table 1 and the operating conditions provided in Table 2, the mathematical models equations were implemented in COMSOL Multiphysics.

4.1. Validation of the model

The first step in the study involved validating the models. The CO_2 absorption efficiency under different scenarios was calculated using experimental [34,35] and simulation results for two ILs ([emim][Ac] and [emim][$EtSO_4$]) and two HFMCs (PS and PP).

Figs. 5 and 6 illustrate the CO_2 absorption efficiency profiles over time for [emim][Ac] with PS membranes, and [emim][$EtSO_4$] with PP membranes, respectively. In the case of using [emim][Ac] with PS membranes (Fig. 5), the system reaches a steady state after approximately 50 min, which corresponds to a total computational time of approximately 46 h, achieving an absorption efficiency of around 33.5%. The simulation results closely matched the experimental data, with a coefficient of determination (R^2) of 0.9844 and a root mean square error (RMSE) of 2.1479, indicating excellent accuracy.

Similarly, Fig. 6 shows the absorption efficiency over time for [emim][$EtSO_4$] in a PP HFMC. In this case, the steady state is reached after approximately 70 min, with an absorption efficiency of about 30% at 291 K. Once again, the simulation results aligned closely with the experimental data, yielding an R^2 of 0.9874 and a RMSE of 2.0619, confirming the model's reliability in representing the real process.

The absorption efficiency of CO_2 at different temperatures using [emim][Ac] in both HFMCs (PS and PP) are also evaluated, as shown in Figs. 7 and 8. A strong correlation is observed between the experimental data and simulation results, with an R^2 of 0.9208 and 0.9638, while the RMSE have values of 1.4657 and 1.7078, in all cases.

It has been reported that increasing the operating temperature leads to a reduction in CO_2 solubility in ILs such as [emim][Ac], as noted by Sohaib et al. [37]. This phenomenon is consistent with the general behavior of physical absorption processes, where gas solubility typically decreases with temperature. However, the elevated temperature also contributes to a higher reaction rate between CO_2 and the IL, which can compensate for the loss in solubility and even enhance the overall absorption performance, as demonstrated by Zareiekordshouli et al. [38]. This combined effect is clearly reflected in the simulation results. Fig. 7 illustrates the CO_2 absorption efficiency in the PS HFMC across a range of operating temperatures. As the temperature increases from 291 K to 348 K, the steady-state absorption efficiency improves markedly—from approximately 28.4% to nearly 44.3%. This improvement can be attributed to enhanced mass transfer rates and the accelerated chemical reaction kinetics facilitated by the higher temperature. A similar trend is observed in Fig. 8, which presents the absorption performance of the PP HFMC using [emim][Ac] as the absorbent. In this case, raising the temperature from 290 K to 340 K leads to a substantial increase in CO_2 absorption efficiency, rising from 15.3% to approximately 41.6%. These findings underscore the dual influence of temperature on the CO_2 absorption process. While elevated temperatures generally lead to reduced gas solubility—particularly in physically driven systems—they also

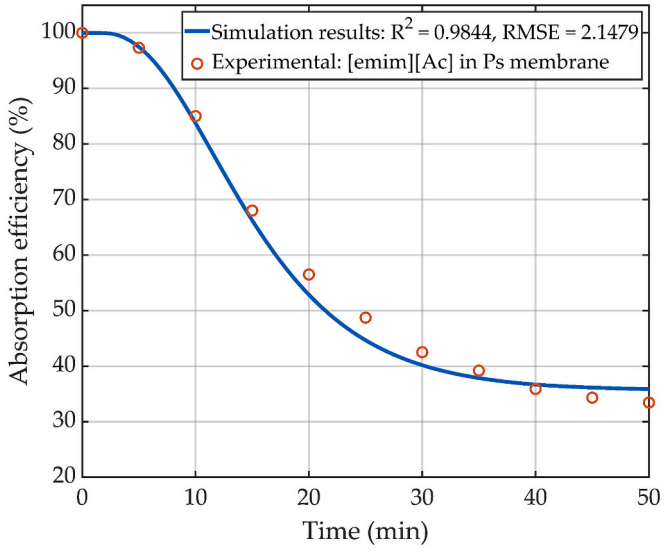

Fig. 5. CO_2 absorption efficiency profile for [emim][Ac] in the PS HFMC at 298 K.

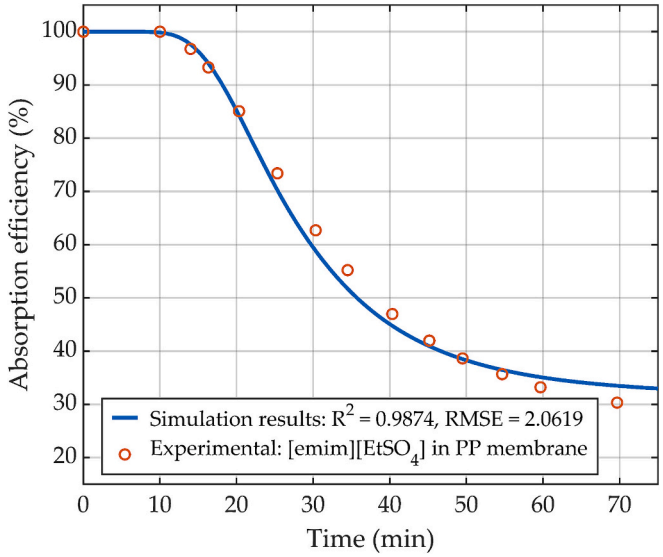

Fig. 6. CO_2 absorption efficiency profile for [emim][$EtSO_4$] in the PP HFMC at 291 K.

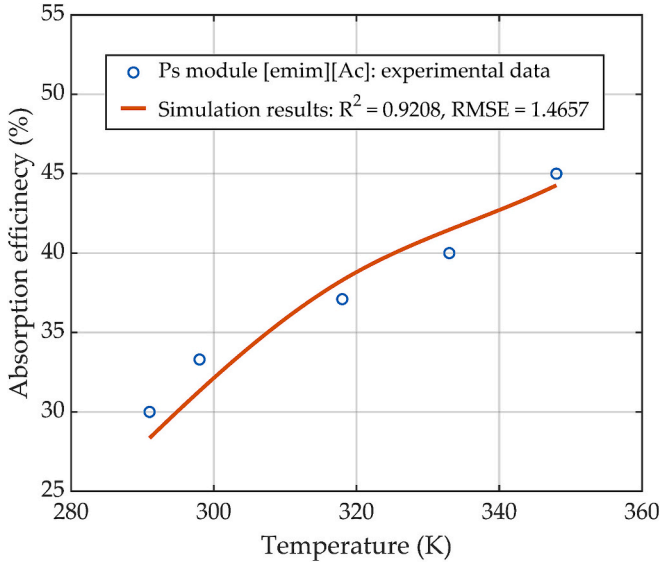

Fig. 7. CO_2 absorption efficiency at different temperatures using [emim][Ac] in the PS HFMC.

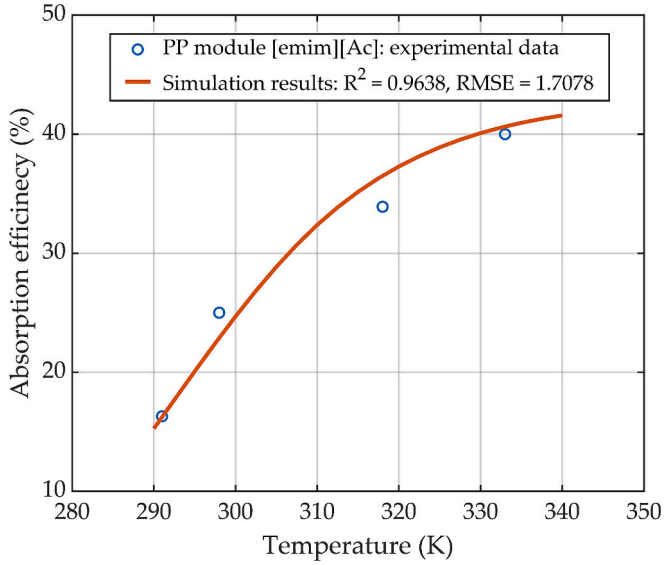

Fig. 8. CO_2 absorption efficiency at different temperatures using [emim][Ac] in the PP HFMC.

enhance the mass transfer coefficient and reaction kinetics, which can significantly benefit chemically reactive systems like those involving IL. It is important to note that temperature also affects other factors, such as viscosity and diffusivity. [emim][Ac] supports both physical and chemical absorption mechanisms, allowing it to maintain and even improve performance at higher temperatures. In contrast, ILs such as [emim][$EtSO_4$], which rely predominantly on physical absorption, exhibits minimal variation in mass transfer behavior with temperature [35]. Therefore, under the conditions studied, the positive impact of increased chemical reactivity and mass transfer outweighs the solubility loss, leading to an overall improvement in CO_2 absorption efficiency.

As shown in Figs. 5 to 8, the mathematical models accurately reflect the CO_2 capture process using [emim][Ac] and [emim][EtSO4] in PS and PP HFMCs over time and across various temperatures, ensuring the reliability of the simulation results presented in this study.

4.2. Velocity and pressure profiles

The cross-section velocity profile of the gas mixture inside the tubes is presented in Fig. 9. A maximum velocity of 1.56 cm/s is observed at the center of the tube, which gradually decreases radially outward. Due

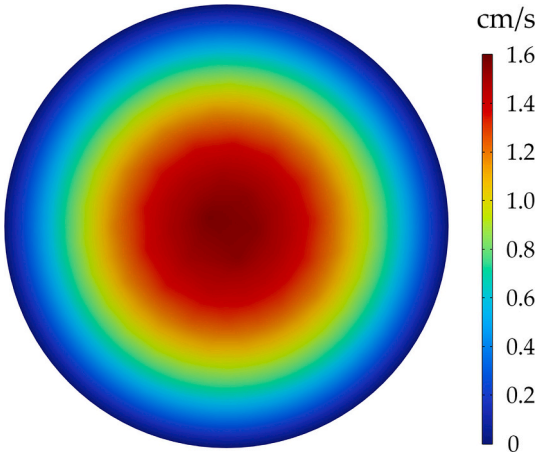

Fig. 9. Cross-sectional velocity profile of the gas mixture inside the tubes (PS module).

to the non-slip condition applied at the membrane walls, the velocity approaches zero at the boundary, where friction between the gas molecules and the membrane surface is the highest. The average velocity of the gas mixture is approximately 0.76 cm/s, corresponding to a gas flow rate of 70 mL/min in the PS HFMC. In comparison, the gas mixture in PP module achieves an average velocity of 1.36 cm/s at the same gas flow rate of 70 mL/min.

The velocity profile of the IL is shown in Fig. 10, depicting a cross-section at the center of the liquid inlet port in the shell. Higher velocities are observed in the middle of the inlet connector (right side of Fig. 10) due to its smaller diameter compared to the rest of the shell. The average velocity of the liquid at the shell inlet is 0.265 cm/s, corresponding to an IL flow rate of 50 mL/min.

The streamlines in Fig. 10 illustrate how the liquid flows across the membranes and fills the shell compartment. As the flow progresses from the inlet (right side of Fig. 10) to the opposite side (left side of Fig. 10), the velocity decreases due to pressure losses caused by friction with the membranes. However, the fluid preferentially follows paths of least resistance, leading to higher velocities in areas with greater spacing between membranes. This imperfect membrane arrangement within the shell results in velocity variations, as indicated by the lighter colors in Fig. 10, which correspond to regions of higher velocity. The 3D model effectively captures the overall fluid flow distribution throughout the shell compartment, providing valuable insights into its behavior.

The pressure drop in the shell compartment for the [emim][Ac] IL in the PS HFMC is shown in Fig. 11. CFD simulations estimate a pressure loss of approximately 97.8 Pa, which aligns closely with values calculated using Ergun's equation. This pressure drop arises from friction with the membranes and shell walls, as well as flow geometry variations caused by changes in membrane spacing. These factors collectively contribute to the observed pressure loss.

4.3. Concentration profiles

Fig. 12 illustrates the CO_2 concentration distribution within the gas mixture as it flows through the tubes and membranes of the PS membrane contactor module when using [emim][Ac]. During the absorption process, the CO_2 concentration decreases progressively along the length of the membranes, starting at 5.66×10^{-3} mol/L at the inlet and dropping to 3.42×10^{-3} mol/L at the outlet.

The reaction of the absorbed CO_2 with [emim][Ac] enhances the driving force for mass transfer, resulting in a steeper concentration gradient between the gas and liquid phases compared to physical absorption alone. As the CO_2 is absorbed and reacts with the IL, the solvent ([emim][Ac]) concentration decreases by approximately 8%, as shown in Fig. 13.

At the beginning of the module (Fig. 13a, L = 0 cm), the [emim][Ac] concentration is nearly uniform in all directions, with a slight reduction observed at the far edge of the shell inlet. This reduction occurs in areas where fresh liquid has difficulty reaching. In regions with larger spacing between the membranes, the convective flow transports liquid more efficiently, leading to higher concentrations of [emim][Ac] (represented by darker colors in Fig. 13b–c).

In contrast, closer to the membranes, a greater proportion of IL reacts with the absorbed CO_2, resulting in a lower [emim][Ac] concentration. This effect is amplified in areas where the flow velocity is slower, indicated by lighter colors. Toward the end of the module (Fig. 13d, L = 11.5 cm), the concentration of the IL undergoes a substantial decline. This phenomenon is primarily attributable to the predominant tendency of the liquid to follow pathways of minimal resistance toward the outlet, thereby leading to the development of a recirculation zone at the far end of the shell. In this region, the replenishment of fresh IL is minimal, while the older, already-reacted solution continues to absorb CO_2, further depleting the available [emim][Ac]. Consequently, the lowest IL concentration is observed in the proximity of the module's outlet. The recirculation and uneven flow distribution are directly linked to the high

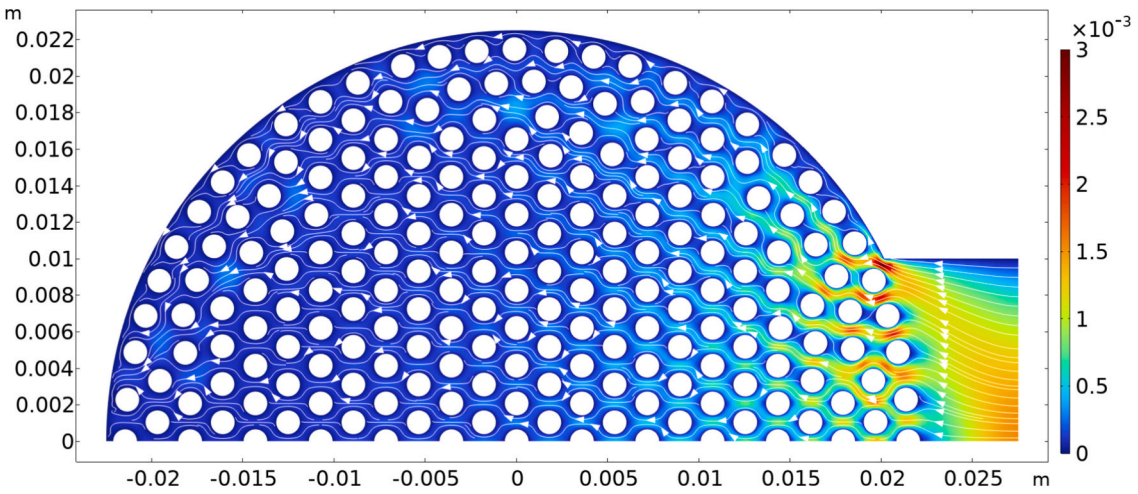

Fig. 10. Velocity profile of [emim][Ac] IL at the shell inlet section (PS module).

Fig. 11. Pressure drop profile in the shell compartment for [emim][Ac] using the PS HFMC.

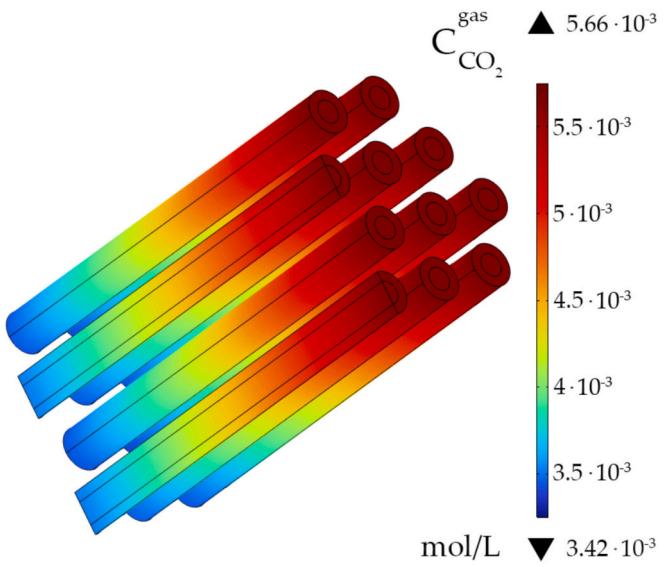

Fig. 12. CO_2 concentration profile within the gas mixture, across tubes and membranes in the PS HFMC with [emim][Ac] at 323.15 K.

viscosity of the IL, which impedes uniform flow and promotes the development of low-velocity regions or dead zones, particularly where convective mixing is limited. These findings underscore the critical necessity to account for viscosity-induced flow behavior when designing the shell side and conducting CFD simulations of HFMC systems to ensure accurate prediction of performance and effective mitigation of mass transfer limitations. When comparing the efficiency of the two ILs, the [emim][Ac] showed better results considering the higher CO_2 solubility.

4.4. Variable gas flow rate

By levering the advantages of COMSOL Multiphysics, the system has been designed for different gas flow rates, as they significantly affect CO_2 absorption efficiency in HFMCs. Fig. 14 illustrates this relationship. For both HFMCs, the absorption efficiency decreases as the gas flow rate increases. This decline is attributed to the reduced residence time of the gas phase within the membranes. The efficiency of using the two membrane types (PS and PP) with [emim][Ac] are assessed at various temperatures (i.e., 290 K, 300 K, 320 K, and 340 K). The gas flow rate is increased from 10 mL/min to 100 mL/min, which represents an increase in the gas velocity from 0.108 m/s to 1.08 m/s, in the case of PS module, and from 0.191 m/s to 1.91 m/s, in the case of PP HFMC, respectively. At a temperature of 340 K, increasing the gas flow rate from 10 to 100 mL/min decreases the absorption efficiency from 96% to about 34.6% for the PS module and from 93.1% to about 30% for the PP HFMC. When the temperature is lowered to 290 K, the same increase in gas flow rate results in a decrease in absorption efficiency from 89.5% to approximately 24.5% for the PS module and from approximately 70.8% to 13.8% for the PP module.

4.5. Variable membrane length

The influence of membrane length on CO_2 absorption efficiency is analyzed using [emim][Ac] IL. The two types of membranes (PS and PP) are evaluated at different temperatures (i.e., 290 K, 300 K, 315 K, and 350 K). The absorption efficiency profiles for [emim][Ac] in PS and PP modules, at different temperatures and membrane lengths are presented in Figs. 15 and 16, respectively.

Increasing the membrane length enhances the mass transfer area between the two phases and extends the residence time of the fluids within the module. In the case of the PS module (Fig. 15), as the membrane length increases, CO_2 absorption efficiency rises from approximately 18.5% at a membrane length of 0.173 m to nearly 87.5%

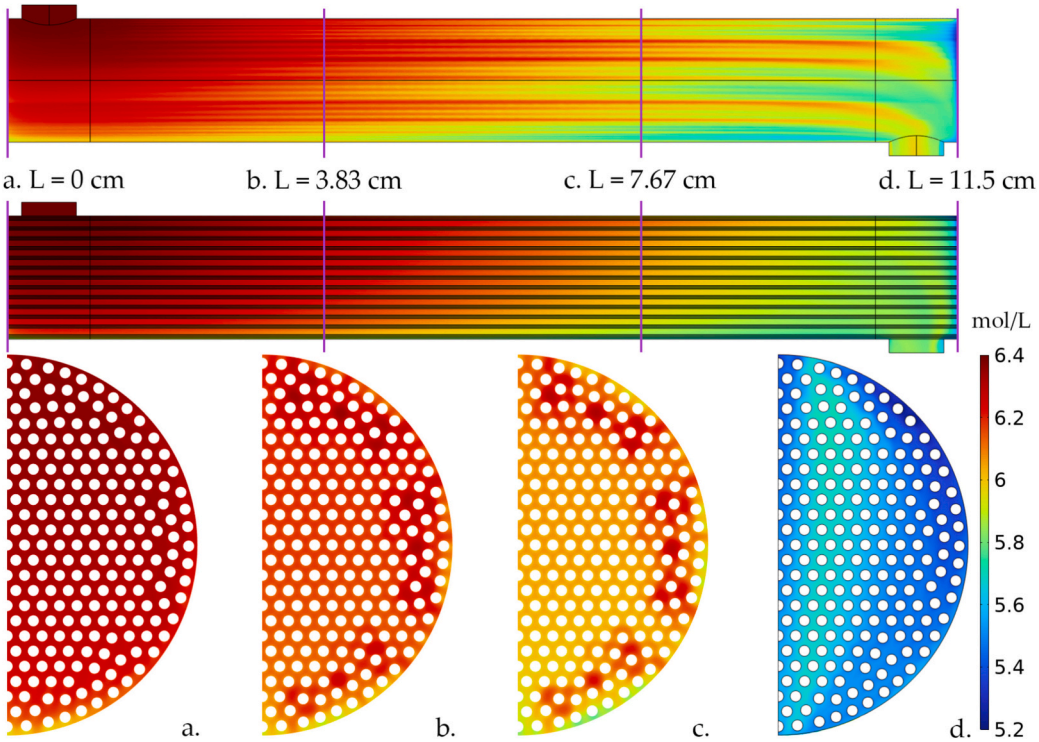

Fig. 13. [emim][Ac] concentration distribution in the shell of the PS HFMC at 323.15 K. (For interpretation of the references to color in this figure, the reader is referred to the web version of this article.)

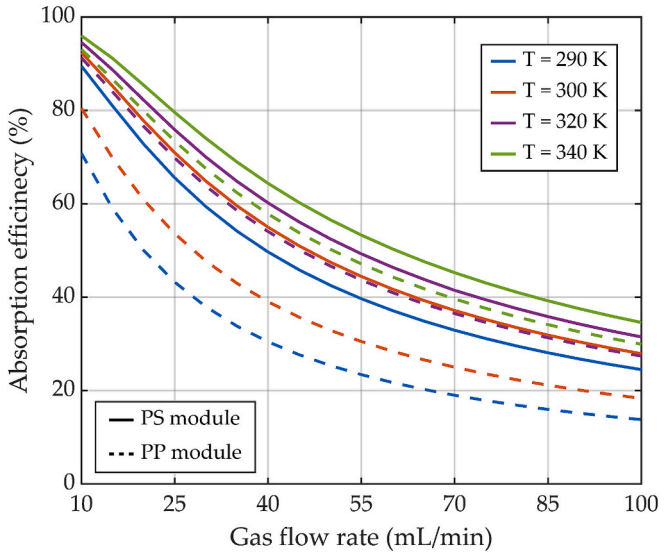

Fig. 14. CO_2 absorption efficiency at different gas flow rates and temperatures using [emim][Ac].

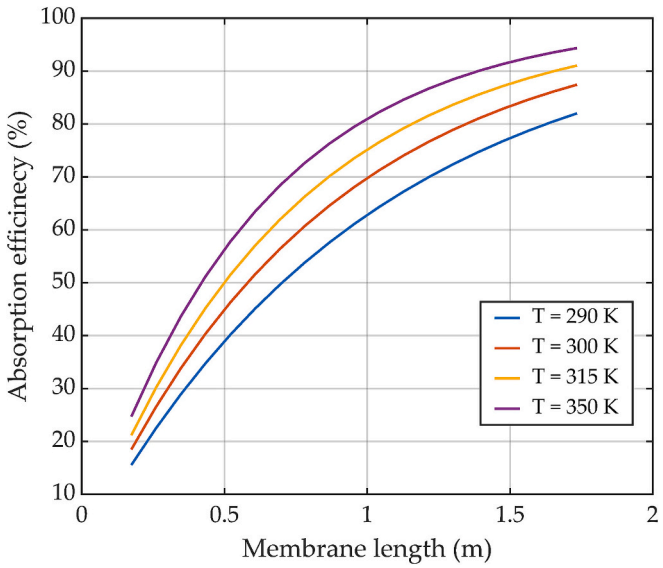

Fig. 15. CO_2 absorption efficiency at different membrane lengths and temperatures using [emim][Ac] in the PS HFMC.

at 1.73 m, when the absorption temperature is 300 K. The increase in temperature further improves the process efficiency for the same membrane length. At 350 K, the efficiency increases from 24.7% to approximately 94.4%. Additionally, simulation results indicate that at temperatures above 310 K, an absorption efficiency exceeding 90% can be achieved using a series of five PS HFMCs with a total length of 1.735 m.

For the PP HFMCs, Fig. 16 shows the variation of absorption efficiency with membrane length at different temperatures when using [emim][Ac]. At 300 K, the absorption efficiency increases by 63.1% when the membrane length is increased tenfold. When the absorption temperature is increased to 350 K, the efficiency rises from 23.8% to approximately 93.8%, when the length is increased from 0.0575 m to 0.575 m. Similarly, using a series of five PP HFMCs, an absorption efficiency of over 90% can be achieved at a temperature higher than 320 K.

4.6. Performance evaluation with shell baffles

Shell baffles are used to intensify the mixing of the liquid in the shell, leading to an increase in the absorption efficiency of the process by minimizing the IL that is simply carried along by the liquid through

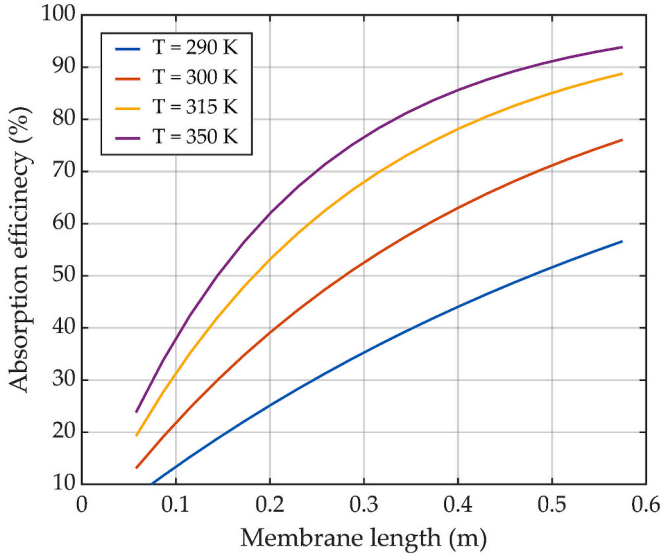

Fig. 16. CO_2 absorption efficiency at different membrane lengths and temperatures using [emim][Ac] in the PP HFMC.

convection. The shell-side bypass effect, observed in the classic membrane contactor [15], can be reduced by using shell baffles. As a result, the driving force of the process, the concentration gradient of CO_2 between the two phases, is increased. A graphical representation of the geometry implemented for the HFMC with shell baffles is represented in Fig. 17. The shell baffles also help stabilize the membranes, minimizing the risk of displacement caused by flow rate fluctuations and ensuring a consistent mass transfer area between the two phases.

Table 4 illustrates how different shell baffle configurations affect the absorption efficiency of CO_2 and liquid pressure drop, in the case of [emim][Ac] IL in PS HFMC. The simulation results were also compared with the value obtained using the Delaware method for pressure drop in Type E shell with baffles [47]. The integration of shell baffles enhances the efficiency of the absorption process but comes at the cost of increased liquid pressure drop. This, in turn, results in higher energy consumption of the pump that transports the liquid. The effect of using a number of ten and twelve shell baffles at different heights (e.g., $0.5 \times D_s$, $0.6 \times D_s$, and $0.7 \times D_s$, where D_s is the inside diameter of the shell), was investigated.

Compared with the classical geometry (without shell baffles), the use of ten baffles with a height half the shell diameter increases the absorption efficiency by 2.2%. However, this improvement is accompanied by an increased liquid pressure drop from 97.9 Pa to about 197 Pa. Using more shell baffles (e.g., twelve), at a higher height (e.g., 70% of shell diameter) results in a further increase in efficiency. However, the pressure drop in the shell drastically increases to about 382.7 Pa, while the absorption efficiency reaches about 39.5%.

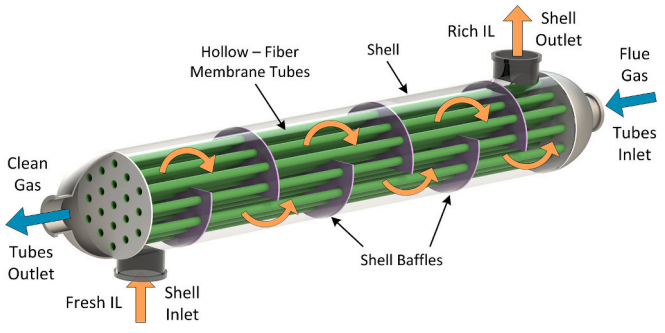

Fig. 17. Graphical representation of the HFMC with shell baffles.

Table 4
Absorption efficiency and shell side pressure drop when using shell baffles.

Number of shell baffles	Height of shell baffles – h_{baffle} (m)	Absorption efficiency (%)	Shell side pressure drop simulation (Pa)	Shell side pressure drop – Delaware method (Pa)	Energy consumption of the pump × 10^4 (W)
0	0	35	97.8	112.2	1.09
10	0.5 × D_s	37.2	197	192.5	2.19
10	0.6 × D_s	37.9	225.9	218.5	2.51
10	0.7 × D_s	38.4	321.2	336.1	3.57
12	0.5 × D_s	38.1	232.6	239.3	2.58
12	0.6 × D_s	38.6	267.8	272.4	2.98
12	0.7 × D_s	39.5	382.7	387.4	4.25

In addition to the pressure drop, the energy consumption of the pump required to overcome this resistance was also evaluated, as shown in the last column of Table 4. The data clearly show that higher pressure drops translate directly into increased pumping energy demand. For the base case without shell baffles, the energy consumption is relatively low, at 1.09×10^{-4} W. When ten baffles at $0.5 \times D_s$ are introduced, the energy consumption nearly doubles to 2.19×10^{-4} W, in line with the rise in pressure drop. As baffle height and number increase, the energy consumption continues to rise. For instance, with ten baffles at $0.7 \times D_s$, the absorption efficiency increases to 38.4%, but the energy demand surges to 3.57×10^{-4} W. Similarly, twelve baffles at $0.7 \times D_s$, which offer the highest efficiency at 39.5%, require the highest energy input, 4.25×10^{-4} W, nearly four times greater than the base case. This clearly demonstrates that the efficiency gains are achieved at the expense of operational energy cost. These findings highlight the importance of conducting a performance-energy trade-off analysis. While higher baffle numbers and heights enhance absorption, the associated rise in pressure drop (and hence energy consumption) may outweigh the benefits, especially in industrial large-scale or long-term operations. Therefore, optimizing the number and height of baffles is essential not only for maximizing absorption but also for ensuring the overall energy efficiency and economic feasibility of the HFMC system.

When increasing the baffle height from $0.6 \times D_s$ to $0.7 \times D_s$ while keeping the number of baffles at 10, the absorption efficiency improves slightly from 37.9% to 38.4%, an increase of just 0.5%. However, this marginal gain comes at the cost of a significant rise in energy consumption, which increases from 2.5×10^{-4} W to 3.57×10^{-4} W, representing nearly a 30% increase. Alternatively, increasing the number of baffles from 10 to 12 while maintaining a baffle height of $0.6 \times D_s$ results in a greater improvement in efficiency, from 37.9% to 38.6% (a gain of 0.7%) with a more moderate increase in energy consumption, from 2.51×10^{-4} W to 2.98×10^{-4} W, or about 16%. This comparison suggests that adding more baffles at a moderate height is a more favorable strategy than increasing the baffle height for the same number of baffles, as it yields a better efficiency-to-energy consumption trade-off.

Fig. 18 illustrates the distribution of liquid pressure drop across the shell for various numbers and heights of shell baffles. The inclusion of vertical baffles leads to a significant pressure drop after each baffle. Moreover, as the number and height of the baffles increase, the overall pressure drop rises.

Fig. 19 presents the liquid-phase concentration distribution of [emim][Ac] within the shell side of the HFMC equipped with vertical baffles. The figure reveals how the IL concentration evolves along the symmetry plane of the module, starting from the shell inlet (left) and

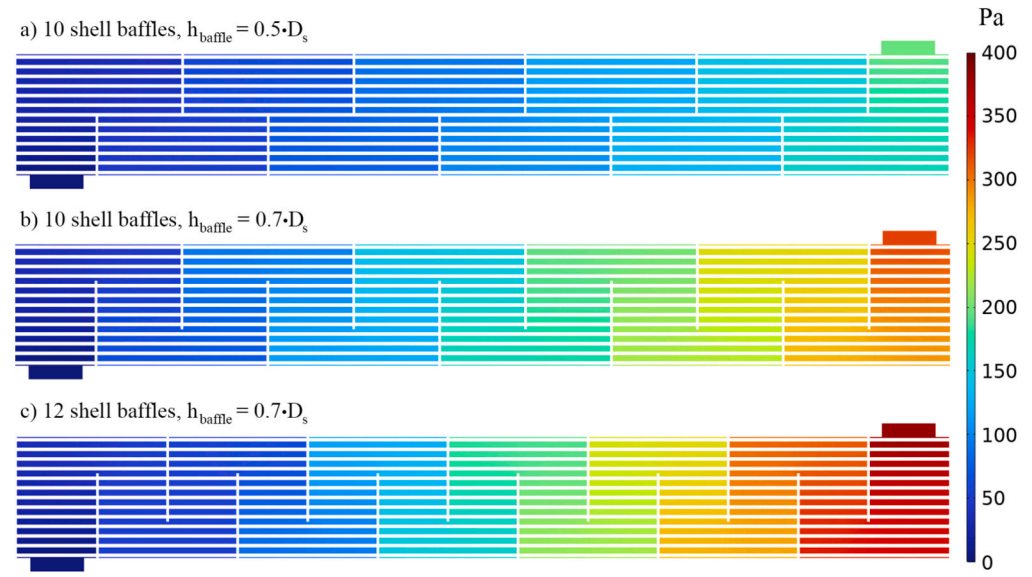

Fig. 18. Liquid pressure drop in the shell of the HFMC with different shell baffles.

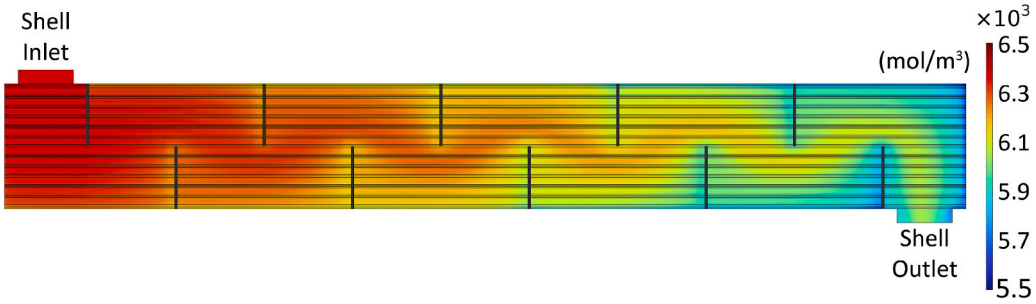

Fig. 19. Liquid concentration field of [emim][Ac] along the shell side of the HFMC with baffles.

progressing toward the shell outlet (right). Unlike the classical HFMC configuration without baffles—where the concentration decreases smoothly and uniformly (as shown in Fig. 13)—the inclusion of baffles introduces distinct patterns and gradients in the concentration field. Specifically, the presence of shell-side baffles leads to periodic mixing and flow disturbances, which cause localized changes in the concentration distribution around each baffle. These flow pattern enhance radial and axial mixing, thereby improving mass transfer between the gas and liquid phases, resulting in an increase absorption efficiency (Table 4). This is evidenced by the alternating high and low concentration zones that develop around of each baffle structure. This spatial variation emphasizes the role of baffles in modifying the transport behavior within the shell side, not only promoting overall efficiency but also creating zones of varied concentration that are critical to understanding and optimizing system performance.

5. Conclusions

This study integrates CFD-based mathematical modeling with prior experimental investigations to analyze the CO_2 absorption process in HFMCs using ionic liquids (ILs). Two types of HFMCs (i.e., PS and PP) with two different ILs (i.e., [emim][Ac]) and [emim][$EtSO_4$]) were used to study the efficiency of the CO_2 absorption process. The CFD models were developed and implemented in COMSOL Multiphysics and validated with experimental data obtained at the laboratory scale. The excellent correlation between the experimental data and the simulation results, with an R^2 value higher than 0.9208 and RMSE lower than 2.1479, confirmed that the models accurately represented the real process.

Due to its high CO_2 solubility, the [emim][Ac] IL showed higher CO_2 absorption efficiencies compared to [emim][$EtSO_4$]. The gas and liquid velocities, as well as concentration profiles, were determined, demonstrating the capability of detailed CFD modeling to calculate process parameters at any point within the system geometry. Furthermore, sensitivity analyses were performed to identify the absorption temperature and membrane length required to achieve an absorption efficiency greater than 90%. The results indicated that a series of five laboratory-scale membrane contactors is required, with an absorption temperature higher than 310 K when using PS HFMC, and 320 K for PP membranes, respectively.

The simulation results demonstrate that incorporating shell-side baffles in HFMCs enhances CO_2 absorption efficiency, with improvements of up to 4.5 percentage points compared to the no-baffle configuration. However, this gain is accompanied by a substantial increase in pressure drop (from 97.9 Pa to nearly 383 Pa), leading to a higher energy consumption for liquid pumping (from 1.09×10^{-4} to 4.25×10^{-4} W). A trade-off analysis revealed that increasing baffle height (e.g., from $0.6 \times D_s$ to $0.7 \times D_s$), at the same number of baffles, results in marginal efficiency gains (0.5%) while causing a disproportionate rise in energy use (nearly 30%). In contrast, increasing the number of baffles (from 10 to 12) at a moderate height ($0.6 \times D_s$) achieves a slightly greater efficiency improvement with only a moderate increase in energy demand (~16%). These results indicate that increasing the number of shell baffles at a moderate height is a more effective approach than simply increasing the baffle height for a fixed number of baffles. This strategy offers a more favorable balance between absorption efficiency and energy

consumption, making it a more efficient and practical design choice for optimizing HFMC performance.

The findings presented in this manuscript are expected to support the scale-up of the entire post-combustion CO_2 capture system based on membrane and IL technology toward commercial implementation. In addition, emerging research trends are centered on several critical areas: the development of cost-effective commercial membrane materials that enhance the durability of contactors and minimize the need for frequent maintenance or replacement; the design of novel absorbents that address thermodynamic limitations by combining high CO_2 solubility and selectivity with low viscosity and cost; and the assessment of system performance under realistic industrial conditions—including gas composition, temperature, and pressure—across sectors such as energy, steel, chemical, cement, and petroleum refining.

Nomenclature

c	Species concentration	mol/m^3
C_p	Specific heat capacity	J/(kg K)
d_i	Inner membrane diameter	m
d_o	Outer membrane diameter	m
D_s	Shell inside diameter	m
D_j	Diffusion coefficient of specie j	m^2/s
h_{baffle}	Height of shell baffles	m
k_0	Reaction constant	1/s
K_H	Henry's coefficient	–
L	Membranes length	m
n	Number of membranes	–
P	Pressure	atm
R_{CO2}	Reaction rate	mol/(m^3 s)
T	Temperature	K
u	Fluid velocity	m/s
Superscripts/subscripts		
i	gas and liquid phase	
j	system components	
Greek letters		
δ_{mem}	Membrane thickness	m
ε_{mem}	Membrane porosity	–
τ_{mem}	Membrane tortuosity	–
φ_{mem}	Packing factor	–
μ	Dynamic viscosity	Pa s
ρ	Density	Kg/m^3
λ	Thermal conductivity	W/(m s)
Abbreviations		
[emim][Ac]	1-Ethyl-3-methylimidazolium acetate	
[emim][EtSO$_4$]	1-Ethyl-3-methylimidazolium ethylsulfate	
IL	Ionic liquid	
HFMC	Hollow-fiber membrane contactor	
PP	Polypropylene	
PS	Polysulfone	

CRediT authorship contribution statement

Alexandru-Constantin Bozonc: Writing – review & editing, Visualization, Investigation, Validation, Formal analysis, Writing – original draft, Software, Conceptualization. **Lucía Gómez-Coma:** Writing – review & editing, Investigation, Validation. **Guillermo Díaz-Sainz:** Validation, Writing – original draft, Conceptualization, Data curation. **Angel Irabien:** Validation, Methodology, Resources, Writing – review & editing, Funding acquisition. **Ana-Maria Cormos:** Methodology, Writing – review & editing, Software, Conceptualization, Supervision, Resources.

Declaration of competing interest

The authors declare that they have no known competing financial interests or personal relationships that could have appeared to influence the work reported in this paper.

Acknowledgments

The authors gratefully acknowledge financial support through projects: CCCDI - UEFISCDI: PN-IV-P8-8.1-PRE-HE-ORG-2024-0228, within PNCDI IV and PLEC2022-009398 (MCIN/AEI/10.13039/501100011033 and European Union Next Generation EU/PRTR).

Data availability

Data will be made available on request.

References

[1] M. Filonchyk, M.P. Peterson, L. Zhang, V. Hurynovich, Y. He, Greenhouse gases emissions and global climate change: examining the influence of CO2, CH4, and N2O, Sci. Total Environ. 935 (2024) 173359, https://doi.org/10.1016/j.scitotenv.2024.173359.
[2] M.F.H. Ismail, A.N. Masri, N. Mohd Rashid, I.M. Ibrahim, S.A.S. Mohammed, W.Z. N. Yahya, A review of CO2 capture for amine-based deep eutectic solvents, J. Ion. Liq. 4 (2024) 100114, https://doi.org/10.1016/j.jil.2024.100114.
[3] K. Storrs, I. Lyhne, R. Drustrup, A comprehensive framework for feasibility of CCUS deployment: a meta-review of literature on factors impacting CCUS deployment, Int. J. Greenh. Gas Control 125 (2023) 103878, https://doi.org/10.1016/j.ijggc.2023.103878.
[4] Y. Yang, W. Xu, Y. Wang, J. Shen, Y. Wang, Z. Geng, Q. Wang, T. Zhu, Progress of CCUS technology in the iron and steel industry and the suggestion of the integrated application schemes for China, Chem. Eng. J. 450 (2022) 138438, https://doi.org/10.1016/j.cej.2022.138438.
[5] J. Du, W. Yang, L. Xu, L. Bei, S. Lei, W. Li, H. Liu, B. Wang, L. Sun, Review on post-combustion CO2 capture by amine blended solvents and aqueous ammonia, Chem. Eng. J. 488 (2024) 150954, https://doi.org/10.1016/j.cej.2024.150954.
[6] M. Eskandari, S.A.N. Khaksar, P. Keshavarz, CO2 absorption using benzylamine as absorbent and promoter in a hollow fiber membrane contactor: a numerical study, J. CO2 Util. 66 (2022) 102287, https://doi.org/10.1016/j.jcou.2022.102287.
[7] P. Gkotsis, E. Peleka, A. Zouboulis, Membrane-based Technologies for Post-Combustion CO2 capture from flue gases: recent Progress in commonly employed membrane materials, Membranes 13 (2023) 898, https://doi.org/10.3390/membranes13120898.
[8] A. Shamiri, M.S. Shafeeyan, H.C. Tee, C.Y. Leo, M.K. Aroua, N. Aghamohammadi, Absorption of CO2 into aqueous mixtures of glycerol and monoethanolamine, J. Nat. Gas Sci. Eng. 35 (2016) 605–613, https://doi.org/10.1016/j.jngse.2016.08.072.
[9] A.M. Dashliborun, F. Larachi, S.M. Taghavi, Gas-liquid mass-transfer behavior of packed-bed scrubbers for floating/offshore CO2 capture, Chem. Eng. J. 377 (2019) 119236, https://doi.org/10.1016/j.cej.2018.06.025.
[10] D.H. Jeong, M.J. Realff, Modular monolith adsorbent systems for CO2 capture and its parameterized optimization, Chem. Eng. Res. Des. 176 (2021) 1–13, https://doi.org/10.1016/j.cherd.2021.09.018.
[11] S. Zhao, P.H.M. Feron, L. Deng, E. Favre, E. Chabanon, S. Yan, J. Hou, V. Chen, H. Qi, Status and progress of membrane contactors in post-combustion carbon capture: a state-of-the-art review of new developments, J. Membr. Sci. 511 (2016) 180–206, https://doi.org/10.1016/j.memsci.2016.03.051.
[12] H. Ruan, S. Wu, X. Chen, J. Zou, J. Liao, H. Cui, Y. Dong, Y. Qiu, J. Shen, Capturing CO2 with NaOH solution from reject brine *via* an integrated technology based on bipolar membrane electrodialysis and hollow fiber membrane contactor, Chem. Eng. J. 450 (2022) 138095, https://doi.org/10.1016/j.cej.2022.138095.
[13] L. Cesari, C. Castel, E. Favre, Membrane contactors for intensified gas-liquid absorption processes with physical solvents: a critical parametric study, J. Membr. Sci. 635 (2021) 119377, https://doi.org/10.1016/j.memsci.2021.119377.
[14] A.-M. Cormos, S. Dragan, C.-C. Cormos, Integration of membrane technology for decarbonization of gasification power plants: a techno-economic and environmental investigation, Appl. Therm. Eng. 205 (2022) 118078, https://doi.org/10.1016/j.applthermaleng.2022.118078.
[15] A. Gabelman, S.-T. Hwang, Hollow fiber membrane contactors, J. Membr. Sci. 159 (1999) 61–106, https://doi.org/10.1016/S0376-7388(99)00040-X.
[16] A. Mansourizadeh, A.F. Ismail, Hollow fiber gas–liquid membrane contactors for acid gas capture: a review, J. Hazard. Mater. 171 (2009) 38–53, https://doi.org/10.1016/j.jhazmat.2009.06.026.
[17] A. Taghvaie Nakhjiri, A. Heydarinasab, O. Bakhtiari, T. Mohammadi, Numerical simulation of CO2 / H2S simultaneous removal from natural gas using potassium carbonate aqueous solution in hollow fiber membrane contactor, J. Environ. Chem. Eng. 8 (2020) 104130, https://doi.org/10.1016/j.jece.2020.104130.
[18] J. Xia, Z. Zhang, L. Wang, F. Wang, H. Miao, H. Zhang, L. Xia, J. Yuan, Performance evaluation and optimization of hollow fiber membrane contactors for carbon dioxide absorption: a comparative study of ammonia, ethanolamine, and diethanolamine solvents, J. Environ. Chem. Eng. 11 (2023) 111354, https://doi.org/10.1016/j.jece.2023.111354.
[19] A. Shiravi, M.S. Maleh, A. Raisi, M. Sillanpää, Hollow fiber membrane contactor for CO2 capture: a review of recent progress on membrane materials, operational challenges, scale-up and economics, Carbon Capture Sci. Technol. 10 (2024) 100160, https://doi.org/10.1016/j.ccst.2023.100160.
[20] J. Palomar, J. Lemus, P. Navarro, C. Moya, R. Santiago, D. Hospital-Benito, E. Hernández, Process simulation and optimization on ionic liquids, Chem. Rev. 124 (2024) 1649–1737, https://doi.org/10.1021/acs.chemrev.3c00512.
[21] Q. Sohaib, J.M. Vadillo, L. Gómez-Coma, J. Albo, S. Druon-Bocquet, A. Irabien, J. Sanchez-Marcano, Post-combustion CO2 capture by coupling [emim] cation

based ionic liquids with a membrane contactor; Pseudo-steady-state approach, Int. J. Greenh. Gas Control 99 (2020) 103076, https://doi.org/10.1016/j.ijggc.2020.103076.
[22] B.F. Goodrich, J.C. de la Fuente, B.E. Gurkan, D.J. Zadigian, E.A. Price, Y. Huang, J.F. Brennecke, Experimental measurements of amine-functionalized anion-tethered ionic liquids with carbon dioxide, Ind. Eng. Chem. Res. 50 (2011) 111–118, https://doi.org/10.1021/ie101688a.
[23] X. Yan, S. Anguille, M. Bendahan, P. Moulin, Ionic liquids combined with membrane separation processes: a review, Sep. Purif. Technol. 222 (2019) 230–253, https://doi.org/10.1016/j.seppur.2019.03.103.
[24] T.J. Simons, P. Hield, S.J. Pas, A novel experimental apparatus for the study of low temperature regeneration CO2 capture solvents using hollow fibre membrane contactors, Int. J. Greenh. Gas Control 78 (2018) 228–235, https://doi.org/10.1016/j.ijggc.2018.08.009.
[25] A. Baghban, A.H. Mohammadi, M.S. Taleghani, Rigorous modeling of CO2 equilibrium absorption in ionic liquids, Int. J. Greenh. Gas Control 58 (2017) 19–41, https://doi.org/10.1016/j.ijggc.2016.12.009.
[26] D. Hospital-Benito, J. Lemus, C. Moya, R. Santiago, J. Palomar, Process analysis overview of ionic liquids on CO2 chemical capture, Chem. Eng. J. 390 (2020) 124509, https://doi.org/10.1016/j.cej.2020.124509.
[27] S. Bazhenov, A. Malakhov, D. Bakhtin, V. Khotimskiy, G. Bondarenko, V. Volkov, M. Ramdin, T.J.H. Vlugt, A. Volkov, CO2 stripping from ionic liquid at elevated pressures in gas-liquid membrane contactor, Int. J. Greenh. Gas Control 71 (2018) 293–302, https://doi.org/10.1016/j.ijggc.2018.03.001.
[28] T. Mulukutla, G. Obuskovic, K.K. Sirkar, Novel scrubbing system for post-combustion CO2 capture and recovery: experimental studies, J. Membr. Sci. 471 (2014) 16–26, https://doi.org/10.1016/j.memsci.2014.07.037.
[29] J.-G. Lu, Z.-Y. Lu, Y. Chen, J.-T. Wang, L. Gao, X. Gao, Y.-Q. Tang, D.-G. Liu, CO2 absorption into aqueous blends of ionic liquid and amine in a membrane contactor, Sep. Purif. Technol. 150 (2015) 278–285, https://doi.org/10.1016/j.seppur.2015.07.010.
[30] J.M. Vadillo, L. Gómez-Coma, A. Garea, A. Irabien, CO2 desorption performance from imidazolium ionic liquids by membrane vacuum regeneration technology, Membranes 10 (2020) 234, https://doi.org/10.3390/membranes10090234.
[31] M.L. Tran, C.H. Nguyen, K.-Y. Chu, R.-S. Juang, A simplified kinetic modeling of CO2 absorption into water and Monoethanolamine solution in hollow-Fiber membrane contactors, Membranes 13 (2023) 494, https://doi.org/10.3390/membranes13050494.
[32] Y. Cao, A. Taghvaie Nakhjiri, M. Ghadiri, CFD investigation of CO2 separation from anesthesia gaseous stream applying novel cholinium lysinate amino acid-based ionic liquid inside the gas–liquid membrane contactor, Eur. Phys. J. Plus 137 (2022) 1044, https://doi.org/10.1140/epjp/s13360-022-03261-x.
[33] S.Z. Islam, M. Arifuzzaman, G. Rother, V. Bocharova, R.L. Sacci, J. Jakowski, J. Huang, I.N. Ivanov, R.R. Bhave, T. Saito, D.S. Sholl, A membrane contactor enabling energy-efficient CO2 capture from point sources with deep eutectic solvents, Ind. Eng. Chem. Res. 62 (2023) 4455–4465, https://doi.org/10.1021/acs.iecr.3c00080.
[34] L. Gomez-Coma, A. Garea, A. Irabien, Carbon dioxide capture by [emim][ac] ionic liquid in a polysulfone hollow fiber membrane contactor, Int. J. Greenh. Gas Control 52 (2016) 401–409, https://doi.org/10.1016/j.ijggc.2016.07.019.
[35] L. Gómez-Coma, A. Garea, A. Irabien, Non-dispersive absorption of CO2 in [emim][EtSO4] and [emim][ac]: temperature influence, Sep. Purif. Technol. 132 (2014) 120–125, https://doi.org/10.1016/j.seppur.2014.05.012.
[36] A.-C. Bozonc, V.-C. Sandu, C.-C. Cormos, A.-M. Cormos, 3D-CFD modeling of hollow-Fiber membrane contactor for CO2 absorption using MEA solution, Membranes 14 (2024) 86, https://doi.org/10.3390/membranes14040086.
[37] Q. Sohaib, M.A. Kazemi, C. Charmette, J. Cartier, M. Younas, A. Azarafza, M. Rezakazemi, J. Sanchez-Marcano, CO2 solubility and diffusivity in 1-ethyl-3-methylimidazolium cation-based ionic liquids; isochoric pressure drop approach, Fluid Phase Equilib. 563 (2023) 113581, https://doi.org/10.1016/j.fluid.2022.113581.
[38] F. Zareiekordshouli, A. Lashanizadehgan, P. Darvishi, Study on the use of an imidazolium-based acetate ionic liquid for CO2 capture from flue gas in absorber/stripper packed columns: experimental and modeling, Int. J. Greenh. Gas Control 70 (2018) 178–192, https://doi.org/10.1016/j.ijggc.2018.02.002.
[39] J. Albo, A. Irabien, Non-dispersive absorption of CO2 in parallel and cross-flow membrane modules using EMISE, J. Chem. Technol. Biotechnol. 87 (2012) 1502–1507, https://doi.org/10.1002/jctb.3790.
[40] A. Nazet, S. Sokolov, T. Sonnleitner, T. Makino, M. Kanakubo, R. Buchner, Densities, viscosities, and conductivities of the imidazolium ionic liquids [Emim][Ac], [Emim][FAP], [Bmim][BETI], [Bmim][FSI], [Hmim][TFSI], and [Omim][TFSI], J. Chem. Eng. Data 60 (2015) 2400–2411, https://doi.org/10.1021/acs.jced.5b00285.
[41] F. Zhang, F. Zheng, X. Wu, X. Yang, Q. Zhang, Y. Yin, Thermophysical properties of [EMIm]ac and its binary and ternary mixtures with water and graphene nanoplatelets for absorption refrigeration, AIP Adv. 9 (2019) 055124, https://doi.org/10.1063/1.5096012.
[42] J. Jacquemin, P. Husson, A.a.H. Padua, V. Majer, Density and viscosity of several pure and water-saturated ionic liquids, Green Chem. 8 (2006) 172–180, https://doi.org/10.1039/B513231B.
[43] L.E. Ficke, H. Rodríguez, J.F. Brennecke, Heat capacities and excess enthalpies of 1-Ethyl-3-methylimidazolium-based ionic liquids and water, J. Chem. Eng. Data 53 (2008) 2112–2119, https://doi.org/10.1021/je800248w.
[44] Q.-L. Chen, K.-J. Wu, C.-H. He, Thermal conductivities of [EMIM][EtSO4], [EMIM][EtSO4] + C2H5OH, [EMIM][EtSO4] + H2O, and [EMIM][EtSO4] + C2H5OH + H2O at T = (283.15 to 343.15) K, J. Chem. Eng. Data 58 (2013) 2058–2064, https://doi.org/10.1021/je400268t.
[45] S. Dragan, H. Lisei, F.-M. Ilea, A.-C. Bozonc, A.-M. Cormos, Dynamic modeling assessment of CO2 capture process using aqueous Ammonia, Energies 16 (2023) 4337, https://doi.org/10.3390/en16114337.
[46] D.W. Green, M.Z. Southard (Eds.), Perry's Chemical Engineers' Handbook, 9th edition, McGraw-Hill Education, 2019. https://www.accessengineeringlibrary.com/content/book/9780071834087 (accessed November 10, 2024).
[47] R.W. Serth, 6 - the Delaware method, in: R.W. Serth (Ed.), Process Heat Transf, Academic Press, Oxford, 2007, pp. 245–275, https://doi.org/10.1016/B978-012373588-1/50009-7.